COMMUNICATION

Biomimetic Anisotropic Reinforcement Architectures by Electrically Assisted Nanocomposite 3D Printing

Yang Yang, Zeyu Chen, Xuan Song, Zhuofeng Zhang, Jun Zhang, K. Kirk Shung, Qifa Zhou, and Yong Chen**

Biological architectures offer inspiration for the design of next-generation structural materials due to their low density, high strength, and toughness through specially evolved structures.[1–8] One of the inspirations originates from superior mechanical properties of naturally evolved composites featured with different orientations of reinforcing fibers or particles (known as Bouligand or twisted plywood structure), for example, the dactyl clubs of peacock mantis shrimp and gigas fish scales, beetle wings, the claws of crab, and lobster.[9–18] The Bouligand structure with ordered collagen or chitin fibers in one layer, yet heterogeneous between different layers, is widely studied and proven to make a great contribution to the reinforcement of crack stopping.[19–21] The crack cannot follow a straight path, thereby increasing energy dissipation and impact resistance. The biological systems grow these reinforcement architectures with best performance through a long-term evolution. However, the complicated architectures in natural materials far exceed the design technology, which hinders the progress of study in reinforcement architectures. Bioinspired reinforced architecture with fibers or ceramic platelets aligned by shear force, magnetic field, or electric field were fabricated by conventional technology and 3D printing[2,22–26] (Table S1, Supporting Information). However, the study of the relationship between the mechanical properties and the rotating angle between aligning direction was not found. Here we present an electrically assisted additive manufacturing/3D-printing technology for the fabrication of reinforcement architecture with anisotropic layers of aligned surface modified multiwalled carbon nanotubes (MWCNT-S). The aligning direction of MWCNT-S in each layer is accurately controlled by a rotation stage and how to use such control to induce improved mechanical properties is studied. Carbon nanotubes (CNTs) have shown great potential as multifunctional nanofillers for polymer-based nanocomposites due to their unique structure and excellent mechanical properties.[27] Controlled alignment of CNTs in polymer matrix by electric field will be studied for further improving the multifunctional properties by using anisotropic properties arising from the extremely high aspect ratio of CNTs.

Additive manufacturing is one of the effective ways to fabricate customized parts with complicated architecture and has a wide application in industry, academia, and daily usages.[28,29] The bioinspired architectures with Bouligand MWCNT-S were designed to enhance the impact resistance as the same for lobster claw and fish scale. The relationship between mechanical property and rotation angles between adjacent layers was studied. Furthermore, this approach is used to mimic the fiber alignment in human meniscus to create reinforced artificial meniscus replica. The meniscus tear is the most common disease that affects more than 1.5 million people through the United States and Europe.[30] The surgery of meniscectomy will increase the risk of osteoarthritis while the meniscus transplantation is restricted by the lack of shortages of donors and tissue mismatch.[31] As a result, artificial substitute for the natural menisci has been proposed as the best solution, which has attracted much attention.[31] Many kinds of meniscal scaffolds were made from polymers (such as polyurethane), silks, and even aligned scaffolds by electrospinning.[32,33] But the biomechanical properties of these scaffolds still need to be improved and the aligned scaffold only partially mimics the circumferential architecture.[34,35] Thus, an optimized design should be developed to fully imitate the wedge-shaped, circumferential, and radial aligned collagen fibrous architecture. Carbon nanotubes are widely used to enhance the mechanical properties in medical devices attributed to their high modulus and biocompatibility.[36] In our study, artificial meniscus was successfully fabricated with radial and circumferential aligned MWCNT-S by electrically assisted nanocomposite 3D printing. The printed meniscus shows enhanced mechanical properties compared

Dr. Y. Yang, Prof. X. Song, Z. Zhang, Prof. Y. Chen
Epstein Department of Industrial and Systems Engineering
Department of Aerospace and Mechanical Engineering
Viterbi School of Engineering
University of Southern California
3715 McClintock Ave, Los Angeles
CA 90089-01932, USA
E-mail: yongchen@usc.edu

Z. Chen, Prof. J. Zhang, Prof. K. K. Shung, Prof. Q. Zhou[+]
Department of Biomedical Engineering
Viterbi School of Engineering
University of Southern California
3650 McClintock Ave, Los Angeles, CA 90089, USA
E-mail: qifazhou@usc.edu

Z. Chen
School of Materials Science and Engineering
Central South University
Changsha, Hunan 410083, China

Prof. X. Song
Department of Mechanical and Industrial Engineering
The University of Iowa
Iowa City, IA 52242, USA

Prof. J. Zhang
School of Power and Mechanical Engineering
Wuhan University
Wuhan 430072, China

[+]Present address: USC Roski Eye Institute, University of Southern California, 1450 San Pablo Street, 90033, Los Angles, USA

DOI: 10.1002/adma.201605750

with native menisci, which serves as a promising replica for the tissue constructs to solve the problem of meniscus tear.

The multifunctionality combined with their robust mechanical properties of Bouligand arranged structures in biological organisms makes them a rich source of inspiration for the design of new materials. The particular examples of Bouligand arranged structures in natural materials are found in the scales of an Arapaima gigas fish and the claws of crab and *Homarus americanus*, which is used either to protect themselves from predating or specifically adapted for close-range combat (**Figure 1**a).[9,37,38] In the claws of *Homarus americanus*, the Bouligand structure is formed by the helicoidal stacking sequence of the fibrous chitin–protein layers (Figure 1a). The presence of the Bouligand arrangement fibers enhances the impact resistance by increasing energy dissipation and fracture toughness.[39] Here we present a method termed as electrically assisted nanocomposite 3D printing that can dynamically align MWCNT-S by controlling a rotating electrical field for the fabrication of bioinspired reinforcement architecture. Instead of a pure MWCNT, MWCNT-S were used to promote the homogeneous distribution in polymer matrix (Figure S1, Supporting Information). Schematic diagrams (Figure 1b), optical microscopy images, and scanning electron microscope (SEM) images (Figure 1c) show the rotating alignment of carbon nanotube bundles to the electric field. Tensile tests show that alignment of MWCNT-S gives rise to an anisotropic elastic modulus compared with random distribution (Figure S2, Supporting Information). The samples possess the highest modulus in the direction that is parallel to the alignment of MWCNT-S and the lowest modulus in the perpendicular direction. The anisotropy is discussed in Figures S2–S6 of the Supporting Information. After the first layer is fabricated, the adjacent layer is gradually rotated about its normal axis, thereby creating Bouligand-type MWCNT-S layers. The cross-section microscopy image shows the same structure with Bouligand-type biological organisms (Figure 1d).

Figure 2a shows the setup process of electrically assisted 3D-printing platform, polymer A (PA, purchased from Maker-Juice)/MWCNT-S nanocomposites were deposited in a transparent glass tank. The photo curable resin (PA) is cured after mask images are projected upward onto the bottom of the substrate by the digital micromirror device (DMD) based projection system.[40–43] A mask-image-projection-based stereolithography (MIP-SL) process is used due to its high-quality surface finish, dimensional accuracy, high fabrication speed, and low machine cost. Different from a laser-based stereolithography (SLA), a DMD is used in the MIP-SL process to dynamically define mask images that are projected on a photo curable resin surface (Figure 2b). Compared with other methods (mechanical forces, shear flows, and magnetic field)[44,45] DC voltage is preferred for its easy processibility and high efficiency in the alignment of carbon nanotubes.[46] Two parallel plate electrodes were used with DC voltages to get the parallel alignment (Figure 2c, gaps 3 cm, 900 V). The alignment relaxation time is determined by $\tau^{-1} = (F(D)/3\eta)G$, $G = \varepsilon_0 \varepsilon E^2/2$, where ε_0 is the electric permittivity of vacuum, η is the matrix viscosity, G is the rotational torque, ε is the anisotropic dielectric constant, and $F(D)$ is the shape factor including aspect ratio D. The relaxation time is in proportional relation with the matrix viscosity. In order to reduce the time for alignment, a photo curable resin with low viscosity (90 cp, 20 °C) is chosen. The alignment of carbon nanotubes in PA/MWCNT-S with 1.5 wt% filler loading takes 60 s. The three key forces that dominate the rotation of carbon nanotubes are torque, coulombic and electrophoresis forces that act on each nanotube due to the electric field (Figure 2d). The polarization of CNT generated by the electric field leads to

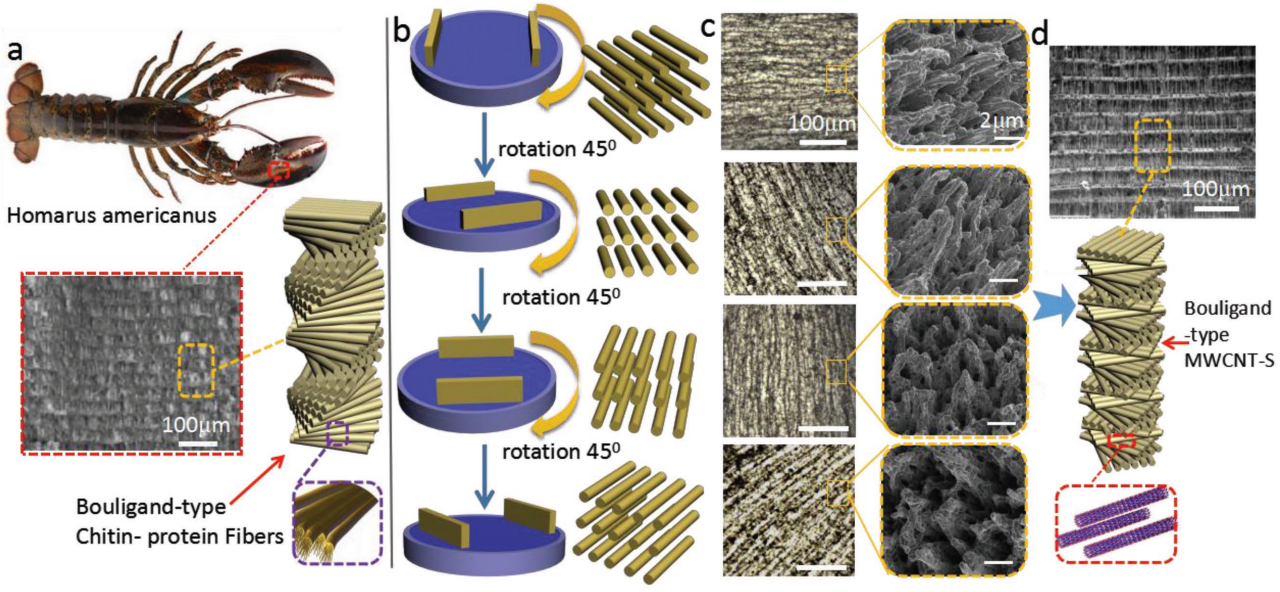

Figure 1. Biomimetic architectures with Bouligand-type MWCNT-S can be recreated by electrically assisted 3D printing. a) The diagram of *Homarus americanus* and the microstructure of claws made with Bouligand-type Chitin-protein fibers. Reproduced with permission.[16] Copyright 2007, Elsevier. b) Schematic diagram of different alignment of carbon nanotubes by the rotation of the electrodes. c) Surface optical microscopy images and SEM images of fracture surface for different alignment of MWCNT-S corresponding to (b). d) Schematic diagram of layer-by-layer bioinspired Bouligand-type MWCNT-S fabricated by the electrically assisted nanocomposite 3D printing.

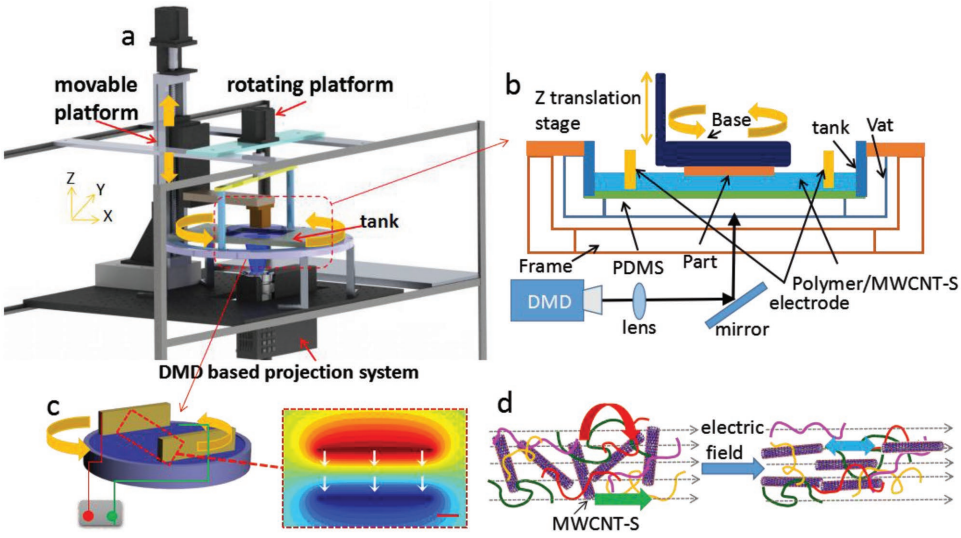

Figure 2. Schematic diagram of the electrically assisted 3D-printing platform for the creation of reinforcement anisotropic composites. a) Diagram of electrically assisted 3D-printing device; the rotation of electrodes is controlled by the platform. b) A bottomup projection process. c) Two parallel electrodes with applied DC electric field and the electrical potential simulated by Comsol Multiphysics. d) Schematic diagram shows rotation of CNT in polymer resin under the application of electric field.

a torque force (red arrow). Coulombic attraction is generated among oppositely charged ends of different CNTs (blue arrow). The electrophoresis force is induced by the presence of charged surface (green arrow).[47]

The simulation by Comsol Multiphysics shows the direction of electric field that controls the alignment of MWCNT-S (Figure 2c). After the first layer is cured, the container with nanocomposites and electrodes is rotated by a stepper motor and the base is moved up for a certain distance (Figure 2b). Hence, when the base is moved down to the container, the alignment of MWCNT-S has been changed due to the controlled rotation of nanocomposites relative to the base to achieve a Bouligand-type structure. An accuracy of 0.5° control of the rotation angle by the motor is designed to study its effects on the impact resistance. Besides, different alignments of carbon nanotubes are successfully achieved by controlling the types of electric field. Figure S11b,c (Supporting Information) shows the simulation of the electric field by using two needle

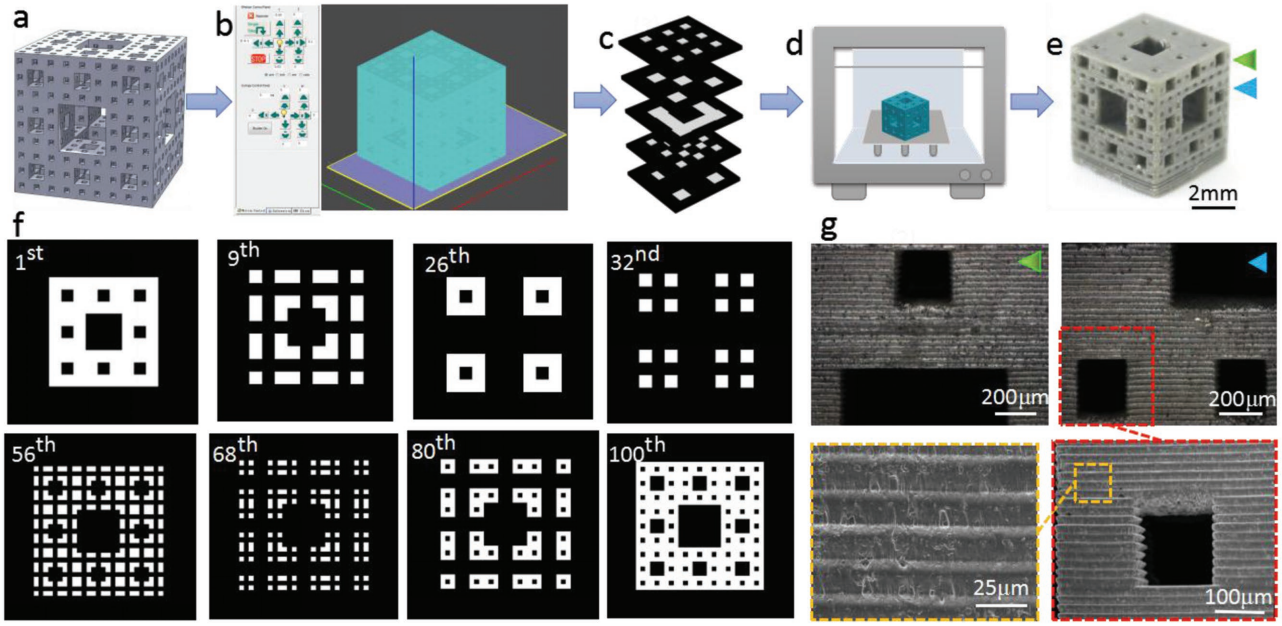

Figure 3. Schematic diagram of the printing process of functional models by electrically assisted 3D printing. a) The Menger sponge model by Solidworks (from Grabcad), b) sliced in our digital micromirror device based Stereolithography (DMD-based SL) software to generate different patterns for projection as shown in (c) and (f). d) The diagram of the electrically assisted 3D printer. e) Photograph of the fabricated Menger model. g) The optical microscopy images of different portions in (e), on the model different colors of triangles are marked with magnified SEM images to show the details.

electrodes and needle-arc electrodes (300 V cm^{-1}), respectively. These two kinds of electrodes will result in circumferential and radial (Figure 5e) alignments of carbon nanotubes.

A Menger structure is designed to demonstrate the electrically assisted 3D printing with Bouligand-type MWCNT-S to enable a new class of strong and lightweight composites. **Figure 3** shows the 3D-printing process of the Menger sponge model by using PA/MWCNT-S composites (see the Experimental Section). The electric field was employed to enable the direction of MWCNT-S during printing. The microscopy images in Figure 3g show that the model (5 mm × 5 mm) was successfully built and the layer thickness is 25 µm. The lengths of squares in the model are 2 mm, 750 µm, and 250 µm, respectively (different colors of triangles are labels that show the microscopy in different portions of the model). The cross-section demonstrates the layer-by-layer fabrication process. The uniformity of the layer thickness shows the control of the electrically assisted 3D printing in building reinforced architectures. SEM images show that there is no defect between layers, which suggests the interlayer bonding is strong.

The Bouligand structure of fibers is shown to enhance the impact resistance under static loading conditions.[17] Here a static compression force was acted on the printed Menger structure with different angles of Bouligand-type MWCNT-S(a smaller Menger model, 2.4 mm × 2.4 mm, with layer thickness of 50 µm) by Instron-5942 to test the ability of impact resistance (Figure S7, Supporting Information). Schematic diagram (**Figure 4**a) shows that the layer starts from $n = 1$ to $n = N + 1$. Each n_{th} layer forms an angle $\alpha_n = (n - 1)\alpha$ with the global x-axis, where n is the layer number and α is the rotating angle formed between adjacent two layers. N layers complete a 180° rotation ($\alpha N = 180°$) through a pitch distance $D = Nd$ (d is the layer thickness). Figure 4b shows three cycles of unit cell repetition along the z-axis for $N = 4$, which shows that the aligned MWCNT-S layer starts from the x-axis with different rotations for following layers and returns to the x-axis at $N = 5$. Figure 4c shows schematic diagram of layered structures for different values of N. For undirectional $N = 1$, the rotation angle is 180°. For $N = 4$, the aligned CNT rotates $\alpha = 45°$ to form the second layer, 90° to form the third layer until it reaches the fifth layer

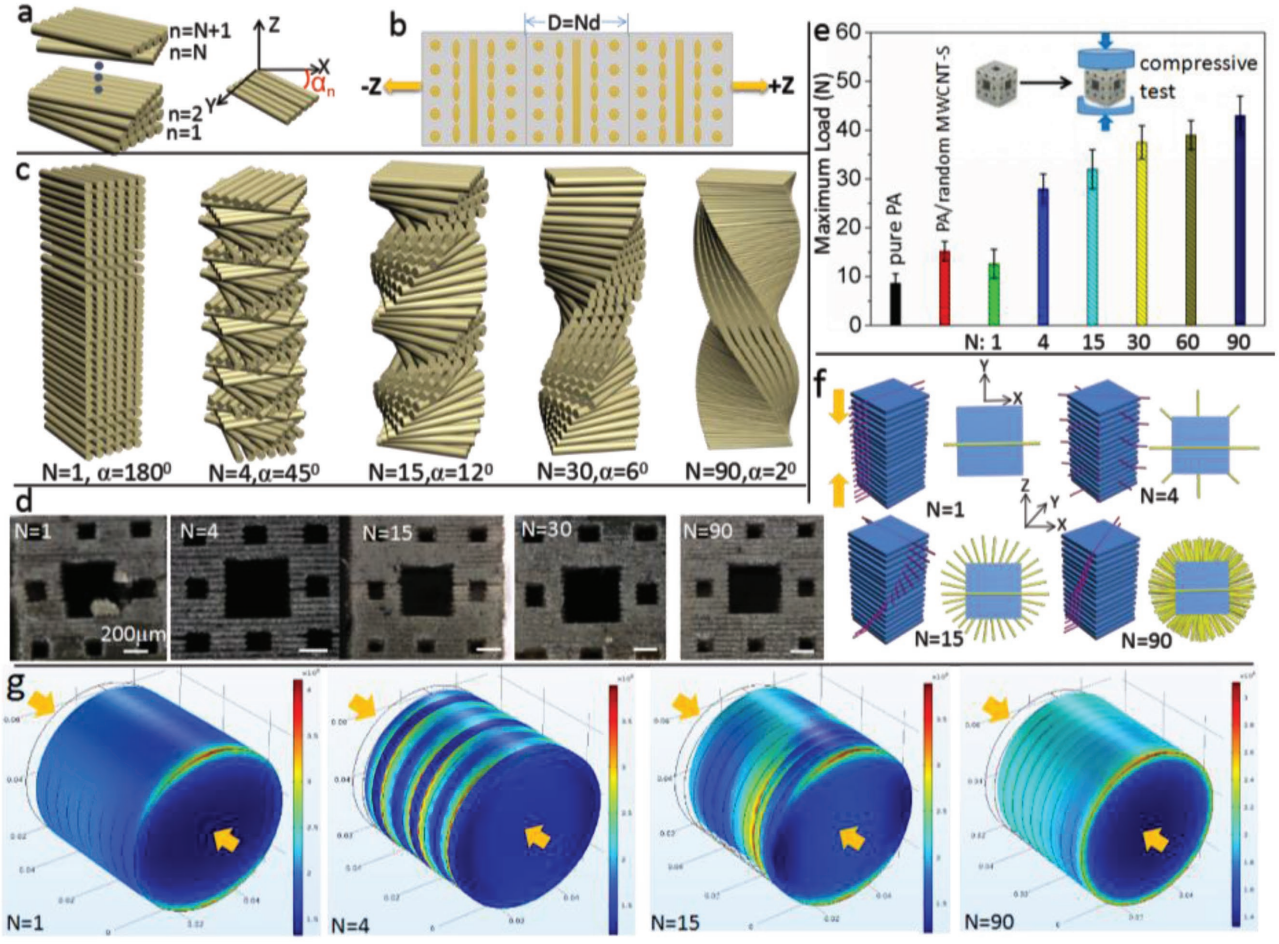

Figure 4. Impact resistance test for Menger models with different rotation angles. a) Diagram of the rotation for different layers. b) Unit cell repetition along the z-axis for $N = 4$. c) Schematic diagram of different types of layered pitch. d) Micrograph of the fraction of electrically assisted 3D printed models by the same compression load (30 N). e) Comparison of load of fracture for the models printed by pure resin, random MWCNT-S, and aligned MWCNT-S with different N values. f) Schematic diagram showing the direction of crack propagation (red lines) and crack arrest (yellow lines) for different rotation angles in the printed structure. g) Simulations by Comsol Multiphysics show the stress distribution for different values of N under the same compression (200 kPa)—arrows show the direction of the force.

to complete a 180° rotation. For $N = 15$, the rotation angle is $\alpha = 12°$, $\alpha = 6°$ for $N = 30$, and $\alpha = 2°$ for $N = 90$. The accurate control of the alignment of MWCNT-S bundles is discussed in Figure S10 (Supporting Information).

The comparison of impact resistance under the same load for different N is shown in Figure 4d. The results show an increased maximum load (the load for initial fracture) with the increment of N (Figure 4e and Figure S7, Supporting Information). The sample will deform in the xy plane under the compression in the z-direction. The schematic diagram in Figure 4f shows the crack lines in each layer under compression. The cracks will follow the path of least resistance (red lines parallel to the alignment of CNT), propagating between aligned CNT rather than severing them. For example, for $N = 1$, if a crack in the matrix occurs in the 0° direction on the bottom layer, the stress concentration will affect the directionality of the damage zone in the second and subsequent layers (see Figure 4g; the stress is concentrated on the red area with the maximum stress higher than 400 kPa). The crack propagation will easily follow the red lines without the need to sever MWCNT-S all through the sample, which leads to catastrophic failure in the compression direction (Figure 4d). Thus the alignment of $N = 1$ leads to a decrease of maximum load even when compared with the random distributed MWCNT-S composites. A quasi-isotropic layup ($N = 4$, $\alpha = 45°$) was chosen as it is an aerospace industry standard design and a robust baseline architecture.[10] Figure 4f shows the rotation of crack propagation direction while the yellow line is perpendicular to the alignment of CNT and represents the direction of crack arrest. With the increment of N, the crack is redirected and twisted through the thickness of the sample, leading to a more tortuous crack path thus greater energy dissipation. The vertical views from the z-direction show that the crack is arrested throughout the xy plane for $N = 90$ compared with only one direction for $N = 1$ (Figure 4f). Through in-plane spreading of cracks and crack redirection, catastrophic propagation of damage through the thickness of the sample is prevented.[48] The studies of compressive strength show that it increases with the increment of N (Figure S8, Supporting Information). This observation is consistent with previous studies that show a wide in-plane spread of damage and

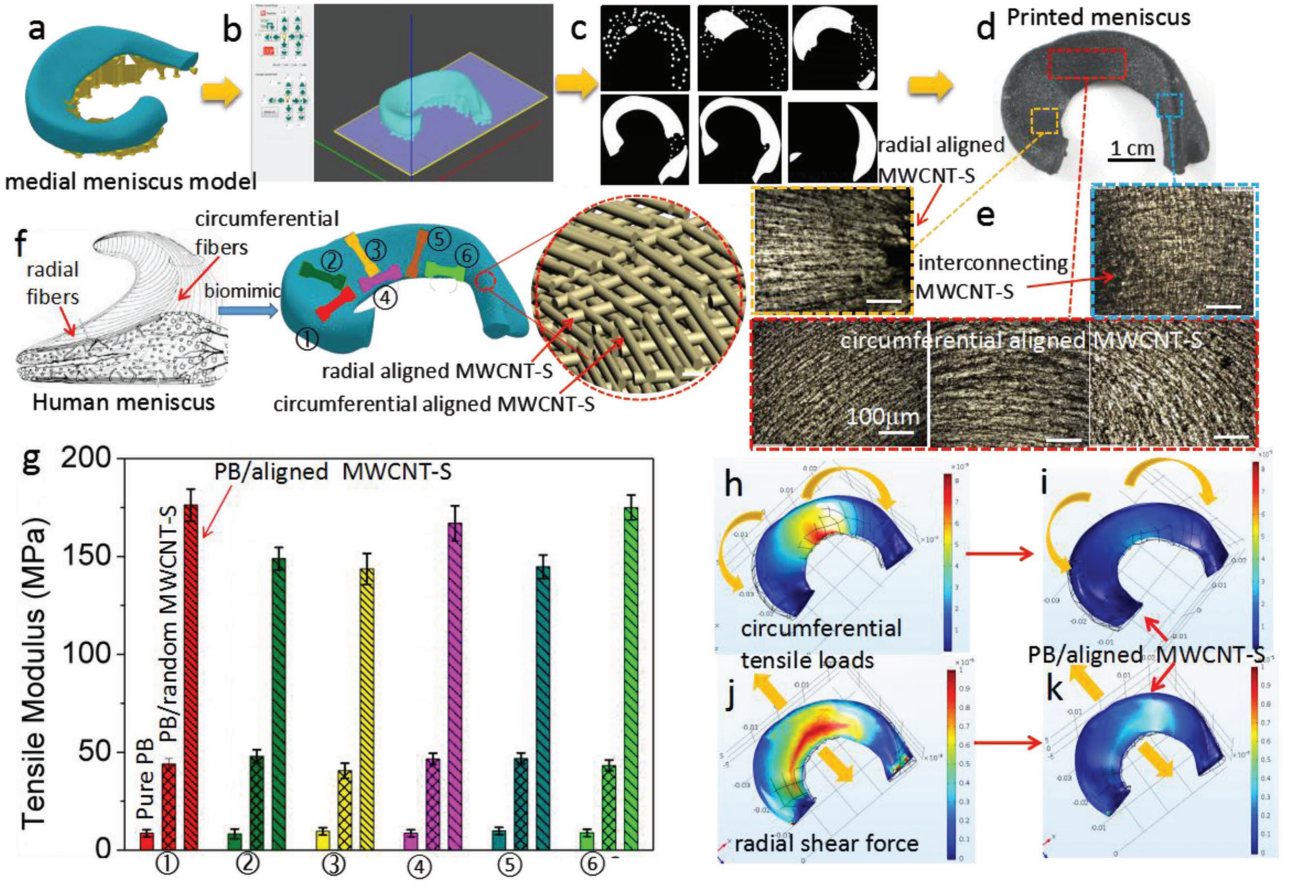

Figure 5. A schematic diagram of artificial meniscus fabricated by electrically assisted 3D printing. a) Model of medial meniscus by Solidworks. b) Model was sliced in the DMD-based SL software to generate different types of patterns (c) for different layers. d) Printed medial meniscus. e) Optical microscopy images show radial and circumferential alignment MWCNT-S for one layer and interconnecting for adjacent two layers. f) Schematic diagram of aligned fibers in Human meniscus. [Reproduced with permission.[54] Copyright 2011, Elsevier] and the biomimic, dog-bone bars for tensile test cut from different parts in the medial meniscus. g) Comparison of tensile modulus in different parts of printed meniscus made by using the pure resin B, PB/random MWCNT-S, and PB/aligned MWCNT-S. Simulation by Comsol Multiphysics to show tears in human meniscus, h) radial tear and j) vertical tear of human meniscus under circumferential tensile loads and radial shear forces, respectively; i,k) the relative strain of the printed meniscus with the reinforcement of aligned MWCNT-S under the same forces.

an increase in stiffness for a smaller fiber rotation angle.[10] No delamination between interlayers is observed after fracture, which indicates the interface area is strong during compression (Figure S8, Supporting Information). A larger pitch length indicates a smaller rotation angle and a larger number of aligned MWCNT-S layers, which result in increased energy dissipation (Figure 4g). Compared with the concentrated stress in $N = 1$, the stress is distributed in various layers ($N = 4$ and $N = 15$) until all through the sample ($N = 90$, Figure 4g). Under a compression of 200 kPa, the maximum stress is 400 kPa for $N = 1$ and decreases to 300 kPa for $N = 90$. Additionally, as elastic properties are a function of fiber angle, the graded design with a larger value of N results in a smooth change in the in-plane stiffness and will reduce the interlaminar shear stresses (a key source of delamination).[49,50] Thus a smaller rotation angle will enhance the ability to withstand greater deflections. Meanwhile, the strain is increased for a large N. This results in a rotating crack front, which yields a large surface area per unit crack length in the direction of crack propagation.

The meniscus plays a crucial role in load bearing and shock absorption, as well as lubrication and nutrition of articular cartilage. The multiple roles leave the menisci susceptible to permanent post-traumatic and degenerative lesions.[51] In recent decades, extensive scientific investigations have been established to study the structure, tear mechanism, and repair solution of meniscus.[52] The mechanical function of human meniscus is dependent on its unique fiber-aligned (circumferential and radial) collagen architecture (**Figure 5**f). Radial (Figure 5h) and vertical (Figure 5j) tears are caused by circumferential tensile and radial shear forces under compression and radial deformation.[52,53] This architecture is interrupted after the meniscus tear and the ability of transmitting load is compromised. Therefore, both the circumferential and the radial modulus should be enhanced for artificial meniscus in order to prevent the failure.

The nature of oriented collagen fibers in native menisci inspires us to solve the problem by mimicking the alignment to achieve enhanced anisotropic mechanical property (Figure 5f).[53,54] Here an artificial meniscus with highly oriented carbon nanotubes (radial and circumferential) was fabricated by electrically assisted 3D printing. Polymer resin B was chosen due to its soft and photo curable properties. Compared with the collagen fiber, carbon nanotubes make greater contributions to the biomechanical properties due to their excellent mechanical property along the direction of the load. Figure 5a–d show the electrically assisted 3D-printing process of medial meniscus with a pair of needle electrodes and needle-arc electrodes (Figure S11, Supporting Information). Circumferential, radial alignments as well as the interconnecting of MWCNT-S between adjacent layers were observed (Figure 5e). Figure 5f shows the schematic diagram of printed medial meniscus; different colors of dog-bone samples show the position on the meniscus for the tensile test. The results show that both the radial and circumferential tensile moduli were enhanced (Figure 5g). The tensile modulus of pure resin B is about 8.7 MPa. With the incorporation of random distributed carbon nanotubes (1.5 wt%), this value is increased to 43 MPa. The results show enhanced circumferential moduli (②, ③, ⑤) of 176 MPa (higher than the circumferential moduli of human menisci (120 MPa)) and radial moduli (①, ④, ⑥) of 143 MPa (three times of the radial moduli of human menisci (48 MPa).[54,55] The enhancement of tensile modulus is attributed to the alignment of carbon nanotubes, which will make a great contribution to prevent the meniscus from failure. Specifically, the circumferential aligned MWCNT-S will prevent the radial tear (Figure 5h,i) and the radial alignment will prevent the vertical tear (Figure 5j,k). The replacement used for meniscus tissue engineering must endure multiple mechanical stresses to provide adequate mechanical support. The stress–strain curves and compressive properties of printed meniscus were studied (Figure S12, Supporting Information). The results show that the printed meniscus has a little higher compressive modulus, higher tensile strength and strain at rupture than human menisci.[56] The compressive modulus (0.79 MPa) is comparable to the human meniscus (0.69 MPa). This result suggests that the printed meniscus can function as a shock absorber and enhance the tear resistance to prolong the life time of usage. The ability for circumventing the crack propagation is important for the biomimetic printed meniscus. Two groups of samples (no precut and precut) prepared with pure Polymer B (PB), PB/random MWCNT-S, and PB/aligned MWCNT-S (with circumferential and radial alignments) were tested. The results (discussed in Figure S13, Supporting Information) show enhanced fracture energy as the interfacial friction between aligned MWCNT-S bundles and polymer matrix and crack deflection. The enhanced modulus and fracture energy demonstrate that the electrically assisted 3D-printed meniscus holds promise as a replica for tissue constructs to circumvent meniscus tear. Besides, 3D printing offers a new way to make customized replacement using computer-aided design models that are individualized to a specific patient and his/her meniscus defect.

Here we propose a way to build a different bioinspired structure by controlling the alignment of MWCNT-S using electric field during 3D printing. The new printing process leads us to an effective approach to the generation of reinforced architectures. Bouligand MWCNT-S reinforced composites provide insight into a toughening mechanism and reveal guidelines for the design of new impact resistant materials. With the precision orientation control of MWCNT-S over the reinforcing architecture, more complex and functional materials created via additive manufacturing will find application in a wide range of engineering disciplines. The potential usage of electrically assisted 3D printed meniscus lies in the combination with computed tomography and magnetic resonance imaging scans to print custom-made individual implants.[57] A photocurable bioink containing cells might also be processed with the proposed approach. The ultimate goal is to mimic the native structure and mechanical properties of the target tissue to develop the printed structures into a functional tissue.

In summary, the electrically assisted 3D printing shows a great promise as a new manufacturing tool to design the reinforced structure for maximized properties, especially for bioinspired architectures. The Menger structures were successfully fabricated with Bouligand-type MWCNT-S to mimic the Bouligand collagen or chitin fibers in nature. The maximum load is profoundly enhanced attributed to the fracture resistance of the Bouligand pattern as shown in natural armor. The results show

that a smaller rotation angle leads to a greater energy dissipation and impact resistance. The study will enable the design of improved engineered biomimetic structural materials. Besides, this work provides a feasible method for printing artificial meniscus with enhanced mechanical performance to prevent the tear disease. The printed menisci will find wide application in the repair of meniscal defects and other fibrous tissues. This electrically assisted 3D-printing technology enables us to design and evolve reinforced architectures with arbitrary 3D geometries and MWCNT-S orientations, which offers tremendous possibilities for applications in aerospace, mechanical, and tissue engineering.

Experimental Section

Surface Modification of MWCNT: 0.5 g of MWCNT-OH (Bucky USA. Inc) was first chemically treated with 30 mL of 10 N sulfuric acid in the presence of 1 g of potassium dichromate for 1 h at 80 °C. It was then filtered and washed with hot and cold water several times to remove the chromic acid and dried in an oven at 90 °C. Then 0.5 mL 3-aminopropyltriethoxysilane dissolved in acetone was added to the carbon nanotube dispersed in water and the stirring was continued for 1 h at 80 °C. The resultant was filtered and washed with acetone (Figure S1a, Supporting Information).

Preparation of Polymer/MINT-S Composite Resin: Polymer resin A (PA) from MakerJuice (MakerJuice Labs, KS, USA) was selected in our study due to its excellent photosensitivity and mechanical property. It contains high tensile epoxy diacrylate (≈9000 psi) and the glycol diacrylate as well as the photoinitiator. This particular resin has a very high tensile strength (63 MPa). MWCNT-S were mixed with polymer resin for 2 h under a magnetic stirring and then ultrasonic bath for 30 min. The composite was degassed in the vacuum before fabrication. PB/MWCNT-S nanocomposite was prepared with the same method.

Electrically Assisted Printing of Polymer A/MWCNT-S Architectures: PA/MWCNT-S nanocomposite was deposited in a transparent glass tank (Figure 2a); the photo curable resin was cured after mask images were projected upward onto the bottom of the substrate by the projector. Two parallel plate electrodes (1 cm × 3 cm) were used with DC voltages to get the parallel alignment. Uniform thin layers were then re-coated by moving the platform to form a desired gap between the previously cured layers and the glass substrate. The container is rotated by a motor after the base is moved up to the highest level. In this case, when the base is moved down to the container, the alignment is changed. Through controlling rotation angles of the container at different layers, Bouligand-type anisotropy can be introduced in the final MWCNT-S reinforced architecture. The resolution of the DMD chip (Texas Instrument, Dallas, TX) is 1024 × 768 and the output light intensity of the projector is 3.16 mW cm^{-2}.

Electrically Assisted Printing of Menger Model: The Menger sponge model was first created using Solidworks (Figure 3a) and then sliced by an in-house developed "DMD-based SL" software (Figure 3b) to get different patterns (Figure 3c,f). Those patterns were then projected to build different layers. For example, the first layer was built by projecting the first pattern until the 100th layer was obtained (Figure 3f). For the fabrication process, different patterns would be projected on the surface of PA/MWCNT-S nanocomposite. The composites would become cured attributed to the photo curable property of the resin. After the first layer was cured on the base, the base would move up and then move down for the second layer to be projected and so on. Rotating nanocomposites with electric field were employed to control the orientation of MWCNT-S related to the base. During the movement, the layer thickness is controlled to be less than the cure depth to make sure that the following layer is stick onto the previous layers. In our study, the movement in the *z*-direction was controlled to be 25–100 μm and the cure depth was about 180 μm for 1 s. Different rotation angles (from 2° to 180°) were used to study its effect on the ability of impact resistance. The curing time of each layer was 10 s and the movement of the base took about 5 s. The alignment of MWCNT-S for 60 s was done in the beginning of the building process and would keep the same orientation afterward. The platform with the electrodes was rotated during the building process to control the MWCNT-S alignment relative to the base. The whole fabrication process took about 25 min for 100 layers. Besides, different models with complicated shapes were successfully fabricated by electrically assisted 3D-printing technology (Figure S9, Supporting Information).

Electrically Assisted Meniscus Printing: Human medial and lateral menisci are wedge shaped and semi-lunar with distinctly different dimensions. Polymer resin B was purchased from 3D Systems. Inc. The best performance with 1.5 wt% loading of MWCNT-S was chosen for the fabrication process. Figure 5a–d shows the electrically assisted 3D-printing process of medial meniscus. Different kinds of electrodes were used for the promotion of circumferential (a pair of needle electrodes) and radial (needle-arc electrodes) alignment of MWCNT-S (Figure S11, Supporting Information). The models by Solidworks were first sliced in the DMD-based SL software (Figure 5b) to generate different types of patterns for different layers (Figure 5c). Medial meniscus was printed with pure resin B and PB/aligned MWCNT-S nanocomposites (Figure 5d). The circumferential alignment was controlled by a pair of needle electrodes to get the first layer, after that the voltage was shut down, then the radial alignment on the second layer was achieved by applying a DC voltage on the two needle electrodes. In this case, two types of alignment of MWCNT-S were got by alternatively applying the DC voltages. The artificial menisci with both types of aligned MWCNT-S were successfully fabricated by the electrically assisted 3D-printing process.

Test of Mechanical Properties: A smaller Menger model was fabricated with dimension 2.4 mm × 2.4 mm in order not to exceed the maximum load of the testing machine. The fabrication process was the same as the Menger model with dimension of 5 mm × 5 mm. A universal testing machine (Instron 5492 Dual Column Testing Systems, Instron, MA, USA) was used. Before the test, the sample was put in the middle of the test plate with the compression force vertical to the alignment of MWCNT-S. The static compression was chosen and the velocity of compression is 1 mm min^{-1} with a maximum compression distance of 2 mm. The pictures from the side view were instantly taken after the test by an optical microscopy. Slices of the printed meniscus were cut into tensile samples using a 3D printed dumb bell shaped punch (central width 3 mm and central length 10 mm.) Six different meniscal specimens were tested to represent different meniscal regions (Figure 5f). In the tensile tests, the velocity of extension is 2 mm min^{-1} with a maximum extension of 3 mm at room temperature. In all of tests, five samples with the same alignment were tested to reduce the experimental error.

DC voltages were applied by using Model 210-02R high-voltage power supply. Fourier transform infrared spectroscopy (FTIR) spectra were collected by using an FT/IR 420 Fourier transform infrared spectrometer. The optical images were obtained on a Micro Vu Sol 161 microscope. SEM images of fracture cross-section of printed Menger model were taken by using JSM-6610LV scanning electron microscope.

Simulation by Comsol Multiphysics: No sliding was observed between the sample and the clamp plates during the compression test. Compression was modeled by clamps with fixed boundary conditions on the bottom and a compression of 200 kPa on the top. The model was designed by Solidworks and then imported to Comsol Multiphysics. Ten layers were fabricated and the material was chosen orthotropic for each layer and the modulus was defined from our test results. Different rotating coordinates were applied on each layer, as such, the rotating angles (0°, 45°, 12°, and 2°) can be chosen according to our design. For example, in Figure 4g, the rotation angle is 180° for $N = 1$. For $N = 4$, the rotation angle is 45°, thus, the third layer rotates 90° until the fifth layer to 180°. The relative strain of medial meniscus was simulated by importing the model from Solidworks into Comsol Multiphysics. Circumferential tensile loads and radial shear forces (200 N) were applied on the model to study the deformation, respectively. The modulus of human menisci was used from refs. [52] and [53] to get the representation of meniscus

tear (Figure 5h,j). The moduli used for the simulation of relative strain of printed meniscus (Figure 5i,k) were based on the data from our study.

Supporting Information

Supporting Information is available from the Wiley Online Library or from the author.

Acknowledgements

Y.Y., Z.C., and X.S. contributed equally to this work. The authors acknowledge the support from National Science Foundation (NSF) (Grant Nos. CMMI-1335476 and CMMI 1151191), National Institutes of Health (NIH) (Grant Nos. P41-EB002182 and 1R01HL118650), and China Scholarship Council. The authors also thank Prof. Qiming Wang and Mr. Zheming Gao for their help with the mechanical tests. Thanks to Xiangjia Li and Center for Electron Microscopy and Microanalysis at USC for the SEM images measurement.

Received: October 25, 2016
Revised: December 9, 2016
Published online: February 10, 2017

[1] H. L. Ferrand, F. Bouville, T. P. Niebel, A. R. Studart, *Nat. Mater.* **2015**, *14*, 1172.
[2] F. Bouville, E. Maire, S. Meille, B. V. Moortele, A. H. Stevenson, S. Deville, *Nat. Mater.* **2014**, *13*, 508.
[3] J. Wang, Q. Cheng, Z. Tang, *Chem. Soc. Rev.* **2012**, *41*, 945.
[4] U. G. K. Wegst, H. Bai, E. Saiz, A. P. Tomsia, R. O. Ritchie, *Nat. Mater.* **2015**, *14*, 23.
[5] N. A. Yaraghi, N. G. Zapata, L. K. Grunenfelder, E. Hintsala, S. Bhowmick, J. M. Hiller, M. Betts, E. L. Principe, J-Y. Jung, L. Sheppard, R. Wuhrer, J. Mckittrick, P. D. Zavattieri, D. Kisailus, *Adv. Mater.* **2016**, *28*, 6835.
[6] J. J. Martin, B. E. Fiore, R. M. Erb, *Nat. Commun.* **2015**, *6*, 8641.
[7] H. D. Espinosa, A. L. Juster, F. J. Latourte, O. Y. Loh, D. Gregoire, P. D. Zavattieri, *Nat. Commun.* **2011**, *2*, 173.
[8] J. C. Nawroth, H. Lee, A. W. Feinberg, C. M. Ripplinger, M. L. McCain, A. Grosberg, J. O. Dabiri, K. K. Parker, *Nat. Biotechnol.* **2012**, *30*, 792.
[9] J. C. Weaver, G. W. Milliron, A. Miserez, K. E. Lutterodt, S. Herrera, I. Gallana, W. J. Mershon, B. Swanson, P. Zavattieri, E. DiMasi, D. Kisailus, *Science* **2012**, *336*, 1275.
[10] L. K. Grunenfelder, N. Suksangpanya, C. Salinas, G. Milliron, N. Yaraghi, S. Herrera, K. E. Lutterodt, S. R. Nutt, P. Zavattieri, D. Kisailus, *Acta Biomater.* **2014**, *10*, 3997.
[11] A. Finnemore, P. Cunha, T. Shean, S. Vignolini, S. Guldin, M. Oyen, U. Steiner, *Nat. Commun.* **2012**, *3*, 966.
[12] H. D. Espinosa, A. L. Juster, F. J. Latourte, O. Y. Loh, D. Gregoire, P. D. Zavattieri, *Nat. Commun.* **2012**, *2*, 173.
[13] D. Kokkinis, M. Schaffner, A. R. Studart, *Nat. Commun.* **2015**, *6*, 8643.
[14] S. N. Patek, W. L. Korff, R. L. Caldwell, *Nature* **2004**, *428*, 819.
[15] D. Raabe, C. Sachs, P. Romano, *Acta Mater.* **2005**, *53*, 4281.
[16] P. Romano, H. Fabritius, D. Raabe, *Acta Biomater.* **2007**, *3*, 301.
[17] E. A. Zimmermann, B. Gludovatz, E. Schaible, N. K. N. Dave, W. Yang, M. A. Meyers, R. O. Ritchie, *Nat. Commun.* **2013**, *4*, 2634.
[18] L. Cheng, L. Wang, A. M. Karlsson, *J. Mater. Res.* **2009**, *24*, 3253.
[19] I. M. Daly, M. J. How, J. C. Partridge, S. E. Temple, N. J. Marshall, T. W. Cronin, N. W. Roberts,*Nat. Commun.* **2016**, *7*, 12140.
[20] A. A. Sawalmih, C. Li, S. Siegel, H. Fabritius, S. Yi, D. Raabe, P. Fratzl, O. Paris, *Adv. Funct. Mater.* **2008**, *18*, 3307.
[21] H. O. Fabritius, C. Sachs, P. R. Triguero, D. Raabe, *Adv. Mater.* **2009**, *21*, 391.
[22] L. R. R. Holmes, J. C. Riddick, *J. Miner. Met. Mater. Soc.* **2014**, *66*, 270.
[23] U. G. K. Wegst, H. Bai, E. Saiz, A. P. Tomsia, R. O. Ritchie, *Nat. Mater.* **2015**, *14*, 23.
[24] L. S. Dimas, G. H. Bratzel, I. Eylon, M. J. Buehler, *Adv. Funct. Mater.* **2013**, *23*, 4629.
[25] B. G. Compton, J. A. Lewis, *Adv. Mater.* **2014**, *26*, 5930.
[26] R. M. Erb, R. Libanori, N. Rothfuchs, A. R. Studart, *Science* **2012**, *335*, 199.
[27] L. S. Schadler, S. C. Giannaris, P. M. Ajayan, *Appl. Phys. Lett.* **1998**, *73*, 3842.
[28] S. H. Huang, P. Liu, A. Mokasdar, L. Hou, *Int. J. Adv. Manuf. Technol.* **2013**, *67*, 1191.
[29] W. Gao, Y. Zhang, D. Ramanujan, K. Ramani, Y. Chen, C. B. Williams, C. C. L. Wang, Y. C. Shin, S. Zhang, P. D. Zavattieri, *Comput. Aided Des.* **2015**, *69*, 65.
[30] I. D. Hutchinson, C. J. Moran, H. G. Potter, R. F. Warren, S. A. Rodeo, *Am. J. Sports Med.* **2014**, *42*, 987.
[31] J. Wei, J. Wang, S. Su, S. Wang, J. Qiu, Z. Zhang, G. Christopher, F. Ning, W. Cong, *RSC Adv.* **2015**, *5*, 81324.
[32] B. B. Mandal, S. H. Park, E. S. Gil, D. L. Kaplan, *Biomaterials* **2011**, *32*, 639.
[33] M. Kobayashi, Y. S. Chang, M. Oka, *Biomaterials* **2005**, *26*, 3243.
[34] B. M. Baker, R. L. Mauck, *Biomaterials* **2007**, *28*, 1967.
[35] F. T. Moutos, L. E. Freed, F. Guilak, *Nat. Mater.* **2007**, *6*, 162.
[36] E. M. Gonçalves, F. J. Oliveira, R. F. Silva. M. A. Neto, M. H. Fernandes, M. Amaral, R. M. Vallet, M. Vila, *J. Biomed. Mater. Res. B: Appl. Biomater.* **2016**, *104*, 1210.
[37] S. Nikolov, M. Petrov, L. Lymperakis, M. Friak, C. Sachs, H. O. Fabritius, D. Raabe, J. Neugebauer, *Adv. Mater.* **2010**, *22*, 519.
[38] B. J. F. Bruet, J. Song, M. C. Boyce, C. Ortiz, *Nat. Mater.* **2008**, *7*, 748.
[39] C. Sachs, H. Fabritius, D. Raabe, *J. Struct. Biol.* **2008**, *161*, 120.
[40] Y. Yang, Z. Chen, X. Song, B. Zhu, T. Hsiai, P. I. Wu, R. Xiong, J. Shi, Y. Chen, Q. Zhou, K. K. Shung, *Nano Energy* **2016**, *22*, 414.
[41] Z. Chen, X. Song, L. Lei, X. Chen, C. Fei, C. T. Chiu, X. Qian, T. Ma, Y. Yang, K.K. Shung, Y. Chen, Q. Zhou, *Nano Energy* **2016**, *27*, 78.
[42] Y. Pan, X. Zhao, C. Zhou, Y. Chen, *J. Manuf. Process.* **2012**, *14*, 460.
[43] X. Song, Y. Chen, T. W. Lee, S. H. Wu, L. X. Cheng, *J. Manuf. Process.* **2015**, *20*, 456.
[44] H. Zhao, Z. Zhou, H. Dong, L. Zhang, H. Chen, L. Hou, *Sci. Rep.* **2013**, *3*, 3480.
[45] B. W. Steinert, D. R. Dean, *Polymer* **2009**, *50*, 898.
[46] C. Park, J. Wilkinson, S. Banda, Z. Ounaies, K. E. Wise, G. Sauti, P. T. Lillehei, J. S. Harrison, *J. Polym. Sci., Part B: Polym. Phys.* **2006**, *44*, 1751.
[47] T. Takahashi, T. Murayama, A. Higuchi, H. Awano, K. Yonetake, *Carbon* **2006**, *44*, 1180.
[48] M. A. Meyers, J. McKittrick, P. Y. Chen, *Science* **2013**, *339*, 773.
[49] S. Suresh, *Science* **2001**, *292*, 2447.
[50] T. Apichattrabrut, K. R. Chandar, *Mech. Adv. Mater. Struct.* **2006**, *13*, 61.
[51] M. Tissakht, A. M. Ahmed, K. C. Chan, *J. Orthop. Res.* **1996**, *14*, 778.
[52] A. J. Fox, A. Bedi, S. A. Rodeo, *Sports Health* **2012**, *4*, 340.
[53] M. A. Sweigart, K. A. Athanasiou, *Tissue Eng.* **2001**, *7*, 111.
[54] E. A. Makris, P. Hadidi, K. A. Athanasiou, *Biomaterials* **2011**, *32*, 7411.
[55] M. Tissakht, A. M. Ahmed, *J. Biomech.* **1995**, *28*, 411.
[56] H. N. Chia, M. L. Hull, *J. Orthop. Res.* **2008**, *26*, 951.
[57] H. W. Kang, S. J. Lee, I. K. Ko, C. Kengla, J. J. Yoo, A. Atala, *Nat. Biotechnol.* **2016**, *34*, 312.